CHALMERS
UNIVERSITY OF TECHNOLOGY

Suspended Stripline on Silicon-Membrane for Integrated Terahertz Couplers

Citation for the original published paper (version of record):
Goturu, A., Dornieden, M., Westin, J. et al (2026). Suspended Stripline on Silicon-Membrane for Integrated Terahertz Couplers. IEEE Transactions on Terahertz Science and Technology, In Press.
http://dx.doi.org/10.1109/TTHZ.2026.3683549

Suspended Stripline on Silicon-Membrane for Integrated Terahertz Couplers

A. Goturu, *Graduate Student Member, IEEE,* M. Dornieden, *Graduate Student Member, IEEE,* J. Westin, and J. Stake, *Fellow, IEEE*

***Abstract*—Directional couplers and power-distribution networks are critical components in balanced circuit topologies. At terahertz frequencies, they are commonly implemented using hollow rectangular waveguides. However, these technologies are inherently difficult to scale to shorter wavelengths and to integrate with active devices. This paper describes the design, fabrication, and characterization of a 925 GHz planar branch-line hybrid coupler implemented in suspended stripline technology, with a 3-μm silicon membrane as the supporting substrate. An initial 3-dB coupler design, based on circuit theory, is fine-tuned using full-wave electromagnetic simulations. The coupler is fabricated using microfabrication techniques and characterized between 750 GHz and 1100 GHz in a WM250 waveguide housing using a vector network analyzer. The hybrid shows measured isolation better than 15 dB and amplitude balance better than 1.1 dB over an 18% bandwidth. Electromagnetic simulations of the waveguide-packaged suspended stripline coupler are in good agreement with the scattering-parameter measurements. The use of suspended stripline technology enables the integration of directional couplers with active devices for terahertz balanced-circuit topologies, such as sideband separating mixers.**

***Index Terms*—Directional couplers, hybrids, power splitters, striplines, submillimeter wave circuits, waveguides.**

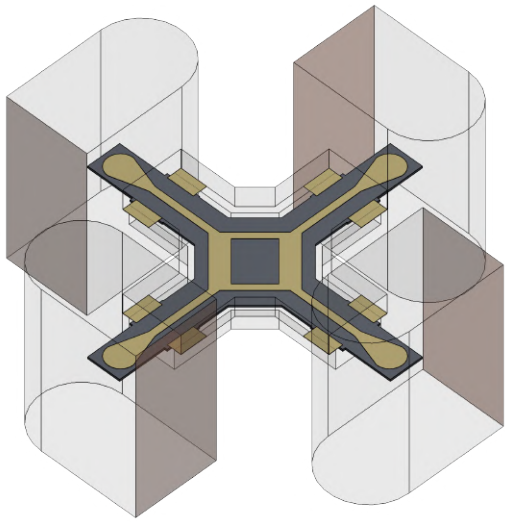

Fig. 1. 3D EM model. Simulation geometry of the coupler presented in this work, in a WM250 waveguide housing. Darkened faces represent simulation reference planes.

I. Introduction

DIRECTIONAL couplers, found at the core of many microwave instruments [1], are commonly implemented as branch-line couplers [2], and realized in various circuit technologies. At terahertz frequencies, above 300 GHz, components are often constructed using a mix of rectangular waveguide technologies, for low-loss transmission, and planar circuits hosting nano-fabricated devices such as diodes [3]. Due to the minuscule scale and tight tolerances of circuit elements, the realization of terahertz components depends on cutting-edge fabrication techniques, which, therefore, impose the upper bound on operating frequency. Despite this, terahertz branch-line couplers using planar technologies remain relatively unexplored, and there is a need to further the development of these couplers to support integrated terahertz components.

Terahertz branch-guide couplers up to a frequency of 1 THz are typically [4] fabricated by direct CNC micro-milling [5] of *E*-plane split rectangular waveguide structures, limiting the maximum achievable aspect ratio, and thus, admittance ratio, to 1:3 [6]. This restriction was relaxed to 1:3.75 through the use of increased-height waveguide sections [7]. Microfabrication techniques [8] also allow the fabrication of higher aspect ratios. However, when scaling such split-block rectangular waveguide components to higher frequencies, the tolerance for mechanical misalignment between the two waveguide halves becomes a limiting factor [9]. Monje *et al*. [10] demonstrated a chip-based coupler that used individual quartz chips with back-to-back *E*-field probes connected by microstrip as the branches in a branch-guide coupler, though alignment of the chips proved difficult with this approach, and the design was deemed impractical to scale to higher frequencies. As an improvement of this method, Zeng *et al*. [11] used a single silicon chip, which addressed the alignment concerns, however, the achievable coupling factor was still limited by the realizable range of the branch impedance. Couplers have also been demonstrated in dielectric waveguide technologies up to 340 GHz [12], and using planar Goubau lines up to

Manuscript received February 13, 2026; revised March 17, 2026. This work was supported in part by the Swedish Research Council (Vetenskapsrådet) under Grant 2020-06187, and in part by the ERC grant (FIRE, 101142356). This research was carried out in the Advanced Digitalization program at the WiTECH Centre CRYTER+, which has been financed by VINNOVA, Chalmers University of Technology, Omnsisys Instruments AB (AAC Omnisys), Low Noise Factory (LNF), Research Institutes of Sweden (RISE) and Virginia Diodes Inc. (VDI).

A. Goturu, M. Dornieden, J. Westin, and J. Stake are with the Terahertz and Millimetre Wave Laboratory, Department of Microtechnology and Nanoscience (MC2), Chalmers University of Technology, SE-412 96 Gothenburg, Sweden.

Color versions of one or more figures in this article are available online at http://ieeexplore.ieee.org. Digital Object Identifier 10.1109/TTHZ.2026.xx

1100 GHz [13]. A disadvantage of both hollow and dielectric waveguide technologies is the difficulty of integrating with electronic circuit components, depending on transitions between the different media [14]. Hesler *et al*. [15] demonstrated the first fully quasi-TEM coupled line coupler at terahertz frequencies, using co-planar transmission lines to achieve realizable coupling factors of up to 7 dB at 750 GHz. As this design does not allow for the realization of higher coupling factors, there remains a need to develop hybrid couplers, with tighter coupling factors, up to 3 dB, that can be practically scaled to higher frequencies.

In this paper, we present a 925-GHz single-section branch-line 3-dB hybrid coupler realized in suspended stripline membrane technology, characterized, through use of *E*-field probe transitions, in a WM250 [16] waveguide housing, from 750 GHz to 1100 GHz. The initial design was presented in 2025 [17]. This paper expands upon this with a detailed design flow, a complete description of the fabrication process, and measurements.

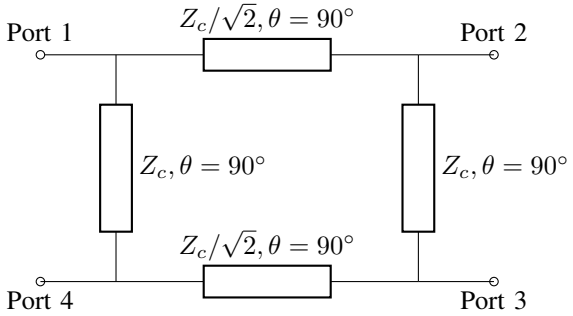

Fig. 2. Equivalent circuit. Ideal 3-dB branch-line coupler represented as a transmission line circuit, consisting of four quarter-wave lines.

II. Method

The ideal 3-dB branch-line coupler [2] can be represented as a transmission line circuit (Fig. 2), consisting of two "through" lines, with characteristic impedance $Z_c/\sqrt{2}$, and two "branch" lines, of impedance Z_c, all having an electrical length of $\lambda/4$ at the design frequency. To realize this circuit in suspended stripline, the parameters for quarter-wave sections of these

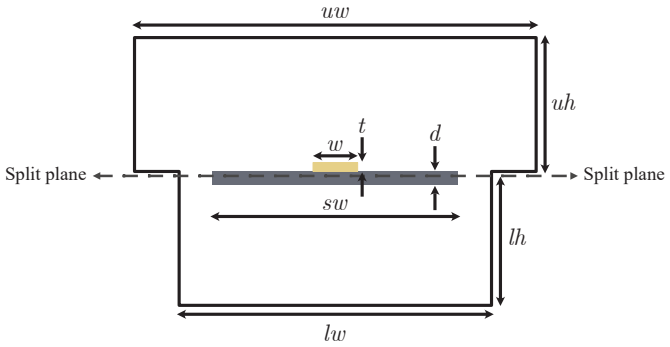

Fig. 3. Stripline parameters and geometry. 2D cross-section of the transmission line supported on a thin membrane, suspended between two machined metal channels joined at the split plane. Impedance is controlled by varying w.

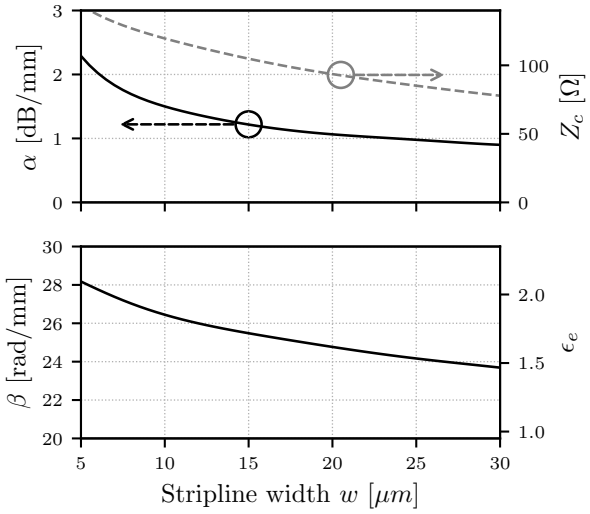

Fig. 4. Simulated stripline parameters. Attenuation constant α, characteristic impedance Z_c, propagation constant β and effective relative dielectric constant ϵ_e of the stripline, simulated at 925 GHz over a realizable range of conductor width w.

lines were determined, and the 3D geometry for the full coupler was then synthesized. In order to characterize the coupler in a WM250 (250 μm $\times$ 125 μm) waveguide test housing, *E*-plane radial probe transition were employed to transition from the quasi-TEM stripline mode to the TE_{10} mode of the waveguide.

A. Design of stripline sections

A suspended stripline cross-section was designed with the geometry as shown in Fig. 3. It's parameters are given in Table I. This geometry supports a fundamental quasi-TEM mode, while the parameters lh, uh, lw and uw were chosen carefully to ensure the next higher order mode was cut off well beyond the WM250 waveguide band.

The propagation characteristics of the stripline were simulated for a range of conductor width, w, using a realistic metal strip conductivity value $\sigma = 2 \times 10^7$ S/m (Fig. 4). As the ratio between through and branch impedances must be $\sqrt{2}$, Z_c was chosen to be 120 Ω, balancing between a through line too wide to realize, and a branch line with too high an attenuation constant.

TABLE I
Suspended Stripline Parameters

Parameter	Value (μm)
$w_{120\Omega}$	10
t	0.5
sw	55
d	3
lh	30
uh	30
lw	70
uw	90

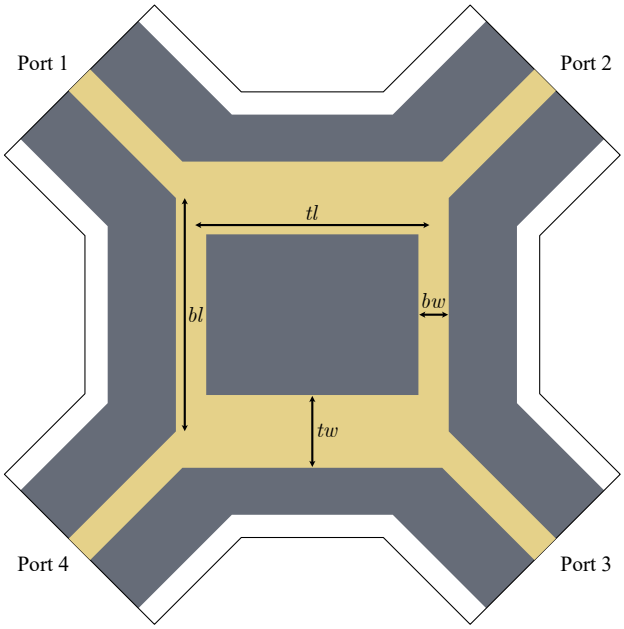

Fig. 5. Circuit layout. Suspended stripline, branch-line coupler after junction compensations. Indicated ports are of the cross section given in Fig. 3, with $w = 120\ \Omega$. Lengths tl and bl are defined between the center lines of the branch and through lines, respectively.

B. Realization of stripline branch-line coupler

The circuit (Fig. 2) was first simulated using ideal transmission-line models, using the chosen Z_c = 120 Ω. A physical realization was then produced using the conductor widths from Fig. 4. To compensate for the size of the junctions, and for the changes in propagation characteristics due to the 3D structure, the widths and lengths of the through and branch lines had to be adjusted in order to achieve similar overall behavior to the ideal model. The final model, after applying the necessary compensations, is shown in Fig. 5, and its optimized parameters are given in Table II.

C. Design of waveguide transition

To embed the suspended stripline circuit within a WM250 waveguide housing, an *E*-field probe transition was designed, based on a radial probe design described by Kooi *et al.* in [18]. Metal beam-leads [19] were integrated into the transition for mechanical support. As these structures altered the impedance of the transmission line slightly (from 120 Ω to 100 Ω), the length of this altered-impedance section was set to approximately a quarter-wavelength at the center frequency (925 GHz), to minimize reflections. The optimized design is shown in Fig. 6. The final membrane circuit of the coupler with transitions is shown in Fig. 1.

D. Electromagnetic simulation

The simulations in this work were performed primarily using two methods: transmission-line models with a linear circuit solver and 3D electromagnetic (3D EM) field simulation. The latter was used to accurately estimate the behavior of the physical circuit, while the former provided a reference for ideal

TABLE II
OPTIMIZATION OF CIRCUIT PARAMETERS

Parameter	Before (μm)	After (μm)
tw	25.5	24.2
tl	65.0	80.0
bw	10.0	10.0
bl	59.4	77.0

circuit behavior. The transmission line sections were modeled as ideal linear circuit components, with $Z_c = 120\ \Omega$; no dispersion or loss was considered for this stage. The 3D EM model was then constructed using the conductor widths from Fig. 4, with the remaining dimensions adopted from Table I.

The 3D EM simulations were performed using a commercial finite-element method based solver. Port parameters, such as characteristic impedance and propagation constant, were retrieved from its 2D port-only solver function, by defining the cross-section geometry. For the presented simulation results, a discrete frequency sweep of 351 points was used, to coincide with the points used later for measurements. The mesh was adaptively refined, until the change in the magnitude of the complex scattering parameters was less than 0.005 between successive meshing passes ($\Delta S < 0.005$), for a solution frequency of 925 GHz. The maximum mesh refinement between iterations was set to 30%, and first order basis functions were used. Four wave ports were used to excite the system. During the course of design iterations, less computationally expensive solver settings were used for quick iteration, 51 frequency points with $\Delta S < 0.02$. Initial designs were produced using ideal boundary conditions: no dielectric loss, silicon dielectric constant of 11.7 [20], and, perfect electrical conductor boundary conditions for all walls and metals. For later simulations, more realistic material parameters were used: metal conductivity of 2×10^7 S/m [21] and high-resistivity silicon with a dielectric loss tangent of 0.0005 [22].

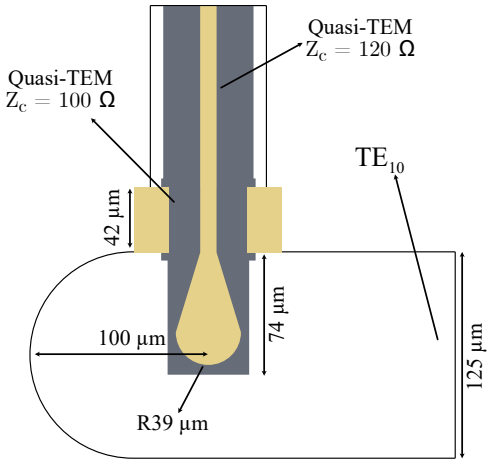

Fig. 6. Waveguide to stripline transition. *E*-plane radial probe to convert between the TE_{10} mode of the WM250 waveguide and the fundamental quasi-TEM mode of suspended stripline.

E. Micro-fabrication of the membrane circuit

The couplers were fabricated from a 4-inch silicon-on-insulator (SOI) wafer that consisted of a 1-μm buried silicon dioxide layer (BOX) separating a 3-μm device layer of high-resistivity silicon ($>10\,\mathrm{k\Omega\,cm}$) from a 300-$\mu$m thick silicon handle layer. This layer structure offers the advantage of having a very selective etch-stop sandwiched between the handle and device layer, allowing for the two silicon layers to be processed essentially independently. The metal traces and beam-leads were fabricated on the frontside of the device layer, following removal of the handle and etch-stop layers. The outlines of the membrane circuit was then defined on the backside of this layer. To remove the handle and etch-stop layers from the backside, the sample must first be temporarily mounted frontside-down to a carrier wafer using a mounting wax.

After removal of the handle layer, the remaining thin silicon device layer becomes very sensitive to a softening and reflow of the mounting wax. A key challenge was thus to perform the etching processes in a cyclic manner and to bake the photoresists at reduced temperatures. A further major difficulty was achieving precise alignment between the frontside structures and the backside-defined coupler outlines. This fabrication process for suspended membrane circuits was inspired by the works that have been carried out in [19], [23], and [24]. The complete process flow is as follows:

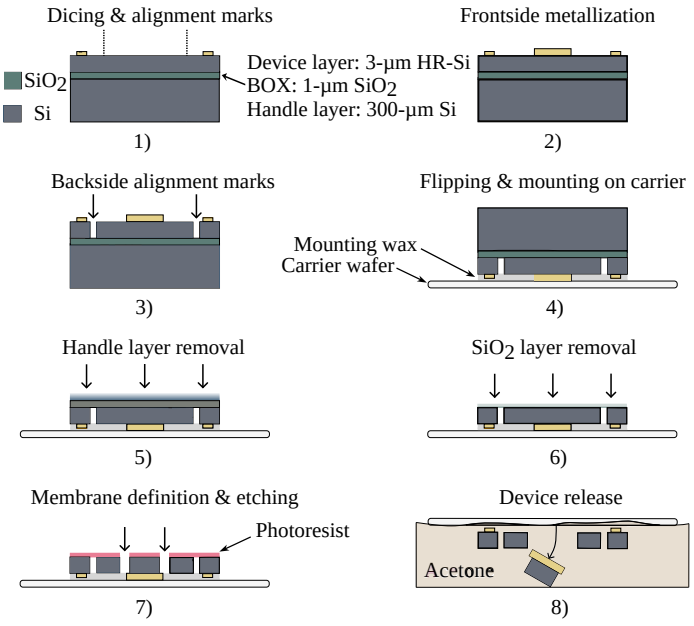

Fig. 7. Process flow. Sequence of processing steps for fabricating and releasing the coupler membrane circuits.

1) *Dicing & alignment marks:* For easier mounting and handling, the wafer was initially diced into chips of 20 mm $\times$ 20 mm size. Using a Raith EBPG 5200 electron-beam lithography (EBL) system, cross-shaped alignment marks (180 μm length and 10 μm width) were patterned into a bi-layer of 700 nm of MMA (methyl methacrylate) EL13 and 70 nm of PMMA (polymethyl methacrylate) A2 e-beam resists that were spin-coated on to the device layer. A Lesker PVD 225 electron-beam evaporator was then used to deposit a 10-nm titanium adhesion layer followed by a 70-nm gold layer with a subsequent lift-off in acetone.
2) *Frontside metallization:* A similar EBL and lift-off procedure was carried out to define the coupler structures and beam-leads. Metallization consisted of a 10-nm titanium adhesion layer followed by 490 nm of gold, both layers again deposited by evaporation.
3) *Backside alignment marks:* The sample was to be mounted on a thick carrier wafer (see below in Step 4), placing the chip outside the focal range of the optics of the backside alignment system, hindering accurate backside-to-frontside alignment. To overcome this issue, marks were etched through the device layer, which were revealed on the processing side after handle layer removal, allowing the use of the more precise frontside alignment procedure. The Heidelberg MLA150 maskless aligner, used for this purpose, provided a frontside alignment accuracy on the order of ± 0.5 μm. To fabricate the etch marks, the gold marks from the first process step were used for alignment, and a second set of cross-shaped marks of the same dimensions were patterned on the device layer in 3.3-μm thick AZ4533 photoresist. This pattern was then etched through the entire 3-μm device layer down to the SiO_2 etch-stop layer using a HBr-based dry etch process in an Oxford PlasmaPro 100 ICP-RIE system.
4) *Carrier wafer mounting:* After fabrication of the etch marks, the chip was flipped and mounted topside-down on a transparent 400-μm thick 4-inch sapphire carrier wafer using (Crystalbond™ 509) mounting wax. To ensure a planar mounting of the chip as well as optimal thermal conductivity during subsequent etching and lithography steps, it was crucial to apply the wax as thinly and uniformly as possible and avoid trapping air bubbles between the chip and the carrier wafer. The solid wax was therefore first crushed into a powder and dissolved in a solution of 80 parts acetone to 20 parts wax by weight. The carrier was placed on a hotplate at the wax reflow temperature of 120 °C and 5 mL of the solution was evenly dispensed in the center of the wafer with a plastic pipette. After allowing the acetone to evaporate for approximately 2 min, the chip was gently positioned with a tweezer on the molten wax film with its frontside facing downwards. The carrier was removed from the hotplate to allow the wax to cool and solidify. Then, the carrier with the mounted sample was placed in a vacuum oven at a temperature of 120 °C and under vacuum of 200 mbar for 30 min. The reflow of the wax, in combination with the vacuum eliminated any remaining air bubbles from below the chip and further improved the planarity of the mounting. Finally, the carrier was removed from the oven and allowed to cool slowly. After reaching room temperature, any excess wax was removed by carefully wiping the carrier and mounted chip with cotton swabs soaked in acetone. The optically transparent sapphire carrier wafer and wax

allowed for a final visual inspection of the mounting quality and detection of any bubbles or voids.

5) *Handle layer removal:* To remove the 300-μm thick silicon handle layer, a SF_6-based dry etch process was carried out in a different Oxford PlasmaPro 100 ICP-RIE system. As the handle layer is thinned down to a remaining thickness of a few micrometers, the 3-μm thin device layer becomes increasingly fragile and highly sensitive to a softening and reflow of the mounting wax, which can easily lead to wrinkling and tearing. Since the wax already begins to soften at a temperature of around 70 °C, the table of the process chamber in the ICP-RIE tool was cooled down to a temperature of 8 °C. In addition, the etch process was carried out in a cyclic manner, with each 30 s etch phase followed by a 30 s pause to allow the sample to cool before the next cycle. The entire process took approximately 3 h to complete. Since the SiO_2 etch-stop layer is optically transparent, etched alignment marks already became visible after the handle layer was fully removed.
6) *BOX layer removal:* A simple buffered oxide etch (BOE) wet etch step was carried out to remove the SiO_2 etch-stop layer. A standard BOE of 7:1 cleared the entire layer in approximately 10 min.
7) *Definition and etching of membrane:* After spin-coating a 3.3-μm layer of AZ4533 photoresist, the MLA150 was used to pattern the membrane outlines on the backside of the chip, aligned to the etch marks. Due to the mentioned sensitivity of the thin device layer, the resist was baked at a reduced temperature of 60 °C in an oven for 2 h. A cyclic HBr-based dry etch process was then carried out in the same ICP-RIE system as for the etch marks, again employing 30 s etch and pause cycles, to etch the coupler outlines through the backside-patterned device layer. For the following release step, a small frame is simultaneously etched around each device to allow acetone to seep in and dissolve the wax.
8) *Device release:* After completion of the final etch step, the finished devices were held in place solely by the mounting wax. To release them, filter paper was placed on the bottom of an acetone-filled beaker and the carrier was immersed into the solvent with the chip facing downwards. Owing to the etched opening frames, the acetone rapidly penetrated and dissolved the mounting wax around every device, allowing the couplers to detach and fall onto the filter paper within only a few minutes. The filter paper containing the collected devices was then transferred to a fresh set of beakers, where residual resist and etch byproducts were cleared through a sequence of cleaning steps using acetone, Remover 1165, and isopropanol. Finally, the devices were left to dry on the filter paper.

F. Micro-milling of the waveguide housing

A waveguide split-block to host the stripline circuit, with access waveguides for characterization, was designed and machined using a 5-axis high precision CNC mill. The two block halves are shown in Fig. 9. The material is CW614N standard brass without any additional coating. The deepest slot has an aspect ratio of 1:1. All critical dimensions of the machined block were measured to be within a ± 2 mum tolerance. A UG-387 precision flange [25] was designed onto each side of the block, to allow mating with the corresponding flange on the VNA frequency extenders.

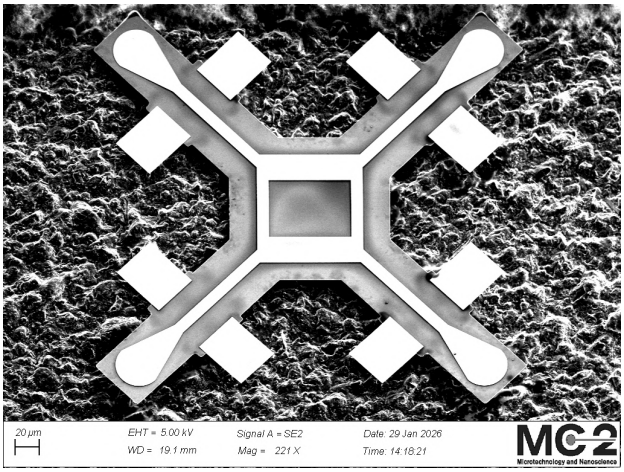

Fig. 8. Silicon membrane circuit. SEM picture of a released device on conductive carbon adhesive tape. The beam-leads were extended beyond the upper channel width uw, to securely hold the membrane in position.

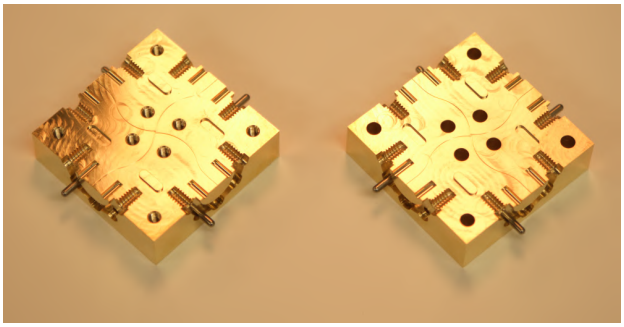

Fig. 9. Machined waveguide housing. The two halves of the channel and access waveguides, along with alignment structures and waveguide flanges. The coupler was first mounted on the bottom block (left), then the second half was placed on top and secured with machine screws.

G. Final assembly

The released membrane circuit was transferred from the filter paper onto the block by submerging it in a drop of water, followed by transferring via a pipette. Once the circuit was on the block, a single hair from a fine-haired paint brush was attached to a micro-manipulator, and used to push the membrane onto the stripline cavity. A 40:60 mixture of isopropanol and water was used to provide a medium for the circuit to glide on. The mounted circuit membrane is shown in Fig. 10. After mounting, the upper block half was positioned on the block and machine screws were used to secure the halves together. Opening and inspecting the block post-measurements confirmed that the membrane was positioned to an accuracy of ± 3 μm within the block.

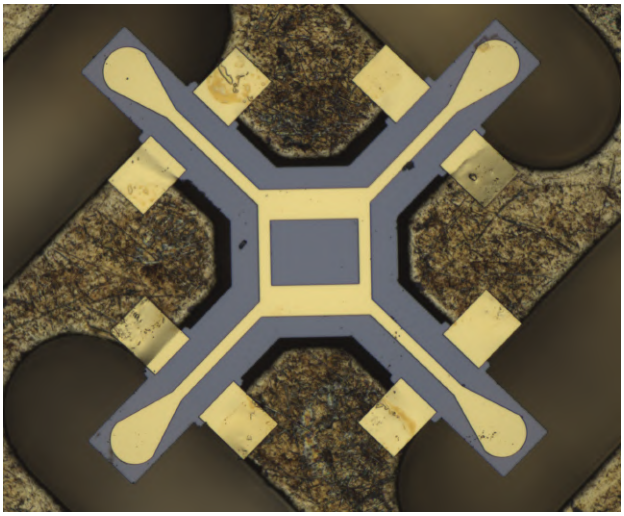

Fig. 10. Assembled coupler. Micrograph of the membrane circuit in the bottom channel block, taken after measurements. The metal beam-leads appear crushed, confirming successful contact between the upper and lower channel walls.

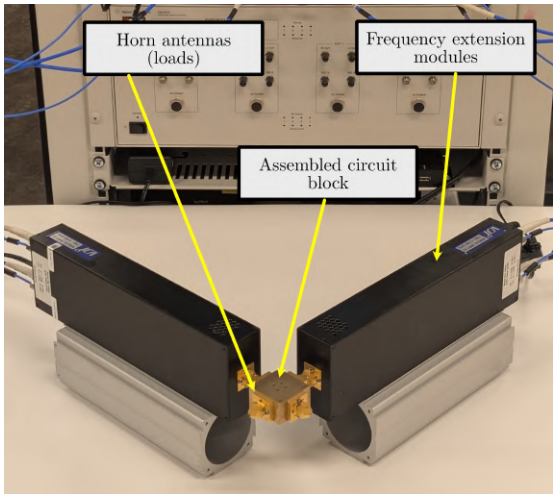

Fig. 11. Measurement setup. Photograph of the VNA, frequency extension modules, and assembled circuit block with matched loads during characterization.

H. Device characterization

The scattering parameters (S-parameters) of the coupler were measured using a Keysight N5242A Vector Network Analyzer (VNA), through a pair of Virginia Diodes VNAX-1.0-mini waveguide frequency extenders. This two-port setup was used to determine the complete S-parameters of the four-port coupler by measuring between pairs of ports, while the remaining two ports were terminated with horn antennas as matched loads. A sweep of 351 points, from 750 GHz to 1100 GHz, was performed with a resolution bandwidth of 100 Hz. No averaging was used. The measurements were referenced to the waveguide flanges on each side of the block.

The VNA was programmed to save uncalibrated S-parameter measurements. Standards for an SOLT calibration [26] were measured before and after measurements. A VNA data processing tool [27] was used to perform off-line calibration and correct the measured S-parameters.

The 18.5-mm access waveguides added significant loss, which was impractical to correct using calibration [28], due to the coupler having 4-ports. Instead, the waveguide loss magnitude was estimated and subtracted based on the reflection measurement results described later. As the stripline cross-section is too small to support any propagation in the waveguide band, the block halves, when assembled without a membrane, act as lossy offset shorts. The return loss seen at the waveguide flange, thus, provides an estimate of the round-trip loss induced by the waveguide. Specifically, for a waveguide of length l, terminated with a short on one end, α can be extracted as:

$$e^{-2\alpha l} = \frac{|S_{11}|}{2l} \tag{1}$$

Due to challenges with flange alignment at these scales [29], the return loss measurements from the empty blocks show a large amount of ripple. To prevent this ripple from obscuring the de-embedded measurements, the standard model for rectangular waveguide attenuation constant [30] was fit to the return loss measurements on all four flanges, producing a smoothed approximation of waveguide loss with frequency. The fit was performed using the least-squares method, by adjusting the effective conductivity (σ) until the sum of squares of the errors between the modeled and extracted α attained a minima. As there are three water lines in this frequency band [31], the regions around these lines were excluded from the fit. The model curve was then used to de-embed the magnitude of S-parameter measurements through the lossy access waveguides.

III. Results and Discussion

Fig. 12 shows the extracted attenuation constant from the empty block measurements, and the fitted model curve. The extracted conductivity, σ = 8.5 $\times 10^6$ S/m, is a factor of two worse than the dc-conductivity from the value specified by the

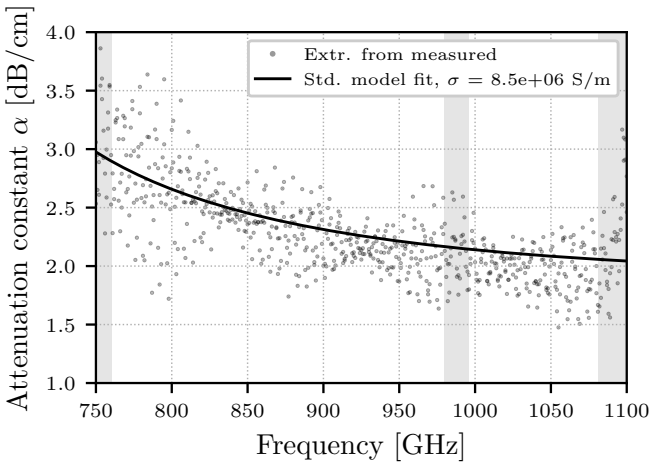

Fig. 12. Access waveguide loss. Extracted attenuation constant from reflection measurements on all 4 ports, assembled without a membrane installed, with the standard waveguide loss model fit. Highlighted regions surround water lines and were excluded from the fit.

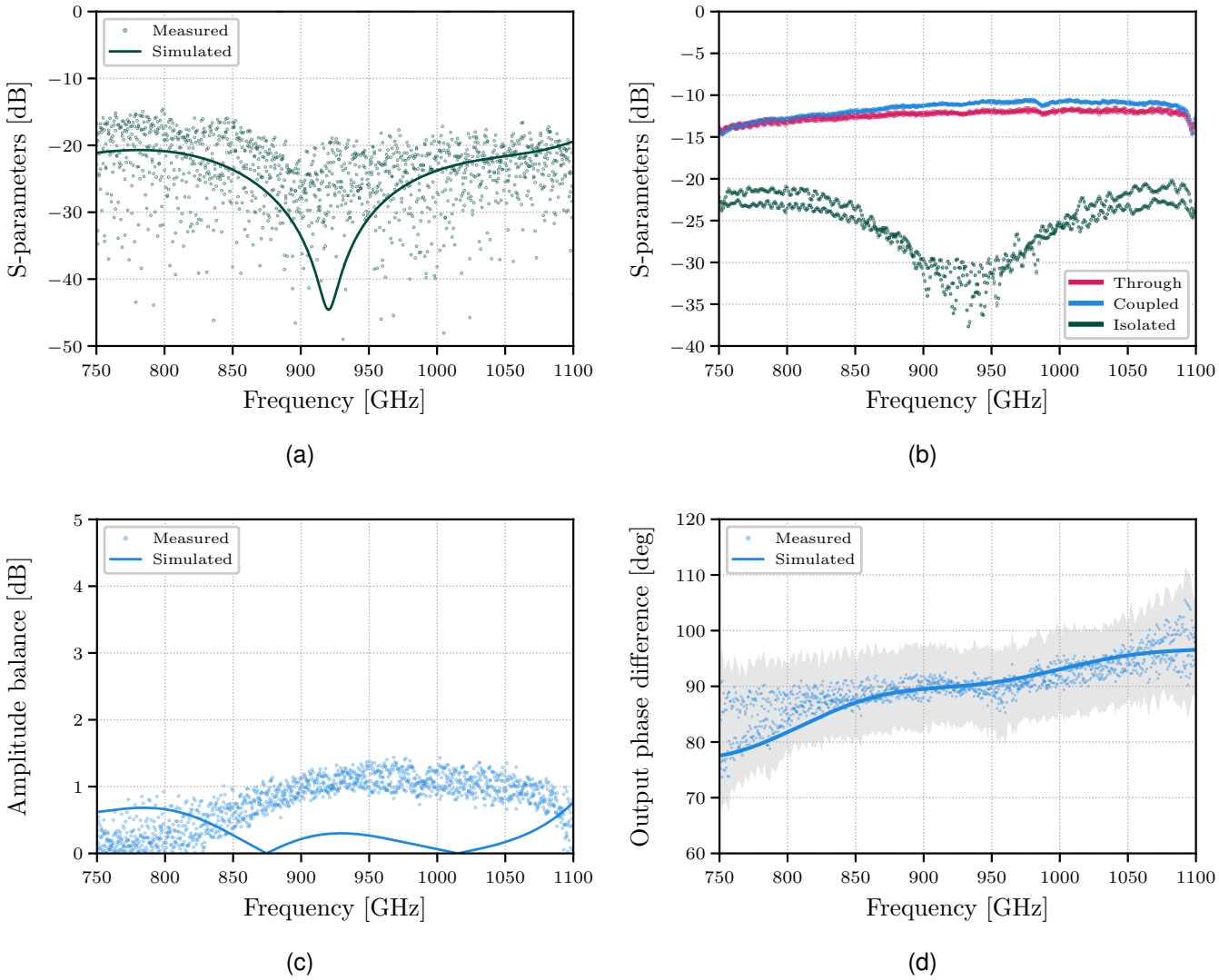

Fig. 13. Scattering parameter measurements. Results from VNA measurements with reference to the outer flanges of the waveguide-packaged suspended stripline coupler, showing a) the reflection coefficient at each port (S_{11}, S_{22}, S_{33} and S_{44}), versus simulated with estimated access loss, b) "through" insertion loss (S_{21}, S_{12}, S_{43} and S_{34}), coupling factor (S_{31}, S_{42}, S_{13} and S_{24}) and isolation (S_{41}, S_{32}, S_{23} and S_{14}), c) amplitude balance, versus simulated, and d) phase difference between outputs, normalized to 90° across the center of the band. Measurements are plotted for all excitation ports. Port numbers are referred to as in Fig. 5.

material vendor (σ = 1.6 $\times 10^7$ S/m). At the center frequency, this corresponds to a very high loss of 4.5 dB per access waveguide. This degraded conductivity also impacts the loss of the coupler itself, and thus, there is a strong indication that performance can be improved by employing a lower-resistivity metal (e.g. CuTe) or coating (e.g. sputtered Au). Simulations show that the through and coupled values could be upto 0.5 dB better with a CuTe block.

The return loss at all ports can be seen in Fig. 13a. It is normal for flange misalignment and aperture size tolerances at the scale of a WM250 waveguide to cause reflections on the order of -20 dB. Thus, as simulations show the device's return loss, with the added access waveguide loss, is likely better than 20 dB across the entire waveguide band, the return loss measured at the flange is mostly representative of the reflections caused the mating waveguide flange itself, and is not a very useful measurement, showing only that there are no strong reflections from the device itself. The remaining raw S-parameter measurements (Fig. 13b) show significantly lower coupled and through power than simulations, as expected, due to the access waveguide loss. These parameters were corrected using the above loss model (Fig. 14), thus showing closer agreement between the simulations and measurement. At the center frequency, the coupling is around 3.4 dB and the through around 4.3 dB, resulting in around 0.9 dB of additional loss over an ideal coupler. These losses can be potentially alleviated through use of more conductive metal walls.

The amplitude and phase balance of a hybrid are key parameters that determine the performance of balanced circuits. The maximum amplitude balance seen is 1.1 dB (Fig. 13c), which is significantly higher than the in-band simulated peak of 0.4 dB. The uncertainty in waveguide loss at each port poses a challenge in de-embedding the amplitude imbalance of the circuit. However, comparing different port excitations

indicates that a major contribution of this imbalance is from the coupler itself. Plotting the phase difference between pairs of output ports showed seemingly random values at the center frequency, ranging from 55° to -78°. This is, however, easily explained by the length of the access waveguides, as even a small change their β, caused by the narrow-wall tolerance [28], results in different electrical lengths for any pair of access waveguides. The VNA also exhibited a significant phase fluctuation, on the order of $\pm 1°$ between sweeps, and phase drift, of around $\pm 6°$ over the course of a full round of measurements. Fig. 13d shows the normalized phase difference between pairs of outputs, where the entire trace is offset with a constant such that the average phase difference between 900 GHz and 950 GHz was 90°. This measurement indicates that the trend in output phase difference versus frequency is comparable to the simulations. Due to the symmetric topology of the circuit, it can be estimated that the true phase balance lies within $\pm 5°$.

IV. Conclusion

We have demonstrated a membrane-circuit, 3 dB hybrid fabricated in a planar suspended stripline technology, utilizing a 3-μm silicon membrane as the supporting substrate, showing an 18% usable bandwidth with isolation better than 15 dB. Balanced mixers employing similar single-section planar couplers have already been demonstrated up to 300 GHz [32]. Further development of planar terahertz components will enable more integrated terahertz front-ends [33].

Acknowledgments

The authors would like to thank the late Dr. Jeffery Hesler for invaluable discussions during the course of this work [34]. We will always cherish his memory and guidance. We also thank Srdjan Aćimović and Omid Habibpour for discussions surrounding micro-fabrication. The membrane circuits were fabricated in the Nanofabrication Laboratory, and the complete coupler module was characterized in the Kollberg Laboratory, both at Chalmers University of Technology, Gothenburg, Sweden.

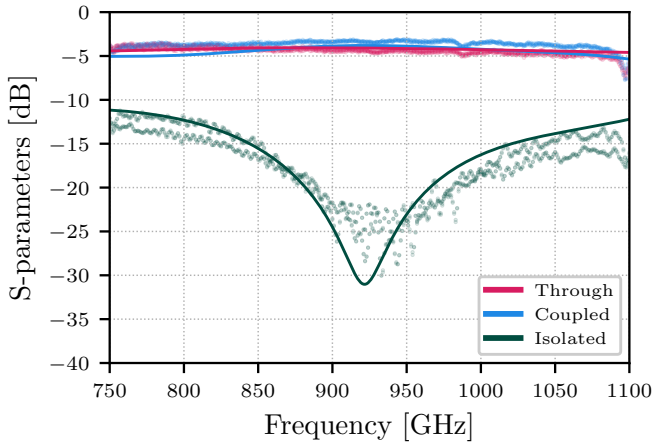

Fig. 14. De-embedded S-parameters. Scattered points are measured magnitude of the "through" insertion loss (S_{21}, S_{12}, S_{43} and S_{34}), coupling factor (S_{31}, S_{42}, S_{13} and S_{24}) and isolation (S_{41}, S_{32}, S_{23} and S_{14}), after subtracting the loss curve modeled in Fig. 12. Measurements are shown for all four excitation ports. Solid lines show EM simulation with $\sigma = 8.5 \times 10^6$ S/m finite-conductivity boundary conditions for the metals. Effective reference plane is as indicated in Fig. 5

References

[1] S. Cohn and R. Levy, "History of Microwave Passive Components with Particular Attention to Directional Couplers," *IEEE Transactions on Microwave Theory and Techniques*, vol. 32, no. 9, pp. 1046–1054, Sep. 1984. doi: 10.1109/TMTT.1984.1132816 .

[2] L. Young, "Branch guide directional couplers," *Proceedings of the National Electronics Conference*, vol. 12, pp. 723–732, 1956.

[3] T. Crowe, W. Bishop, D. Porterfield, J. Hesler, and R. Weikle, "Opening the terahertz window with integrated diode circuits," *IEEE Journal of Solid-State Circuits*, vol. 40, no. 10, pp. 2104–2110, 2005. doi: 10.1109/JSSC.2005.854599 .

[4] A. Khudchenko, M. Fominsky, C. Heiter, S. Heyminck, R. Gusten, B. Klein, R. Hesper, A. M. Baryshev, J. Barkhof, K. Rudakov, D. Montofre, D. Van Nguyen, V. P. Koshelets, and P. N. Dmitriev, "Design and Performance of a Sideband Separating SIS Mixer for 800–950 GHz," *IEEE Transactions on Terahertz Science and Technology*, vol. 9, no. 6, pp. 532–539, Nov. 2019. doi: 10.1109/TTHZ.2019.2939003 .

[5] B. Z. Balázs, N. Geier, M. Takács, and J. P. Davim, "A review on micro-milling: recent advances and future trends," *The International Journal of Advanced Manufacturing Technology*, vol. 112, no. 3-4, pp. 655–684, Jan. 2021. doi: 10.1007/s00170-020-06445-w .

[6] X. Hao, M. Chen, L. Liu, J. Han, N. He, G. Zhao, and N. Chen, "Fabrication of Large Aspect Ratio PCD Micro-milling Tool with Pulsed Lasers and Grinding," *Journal of Manufacturing Processes*, vol. 58, pp. 489–499, 2020. doi: 10.1016/j.jmapro.2020.08.032 .

[7] P. J. Sobis, J. Stake, and A. Emrich, "A 170 GHz 45° Hybrid for Submillimeter Wave Sideband Separating Subharmonic Mixers," *IEEE Microwave and Wireless Components Letters*, vol. 18, no. 10, pp. 680–682, Oct. 2008. doi: 10.1109/LMWC.2008.2003463 .

[8] A. Pavolotsky, D. Meledin, C. Risacher, M. Pantaleev, and V. Belitsky, "Micromachining approach in fabricating of THz waveguide components," *Microelectronics Journal*, vol. 36, no. 7, pp. 683–686, 2005. doi: 10.1016/j.mejo.2005.04.041 .

[9] N. M. Ridler and R. G. Clarke, "Establishing Traceability to the International System of Units for Scattering Parameter Measurements From 750 GHz to 1.1 THz," *IEEE Transactions on Terahertz Science and Technology*, vol. 6, no. 1, pp. 2–11, 2016. doi: 10.1109/TTHZ.2015.2502068 .

[10] R. Monje, V. Belitsky, and V. Vassilev, "A Novel Design of Broadband Waveguide Directional Couplers and 3-dB Hybrids," *IEEE MTT-S International Microwave Symposium Digest*, pp. 1169–1172, 06 2006. doi: 10.1109/MWSYM.2006.249399 .

[11] L. Zeng, W.-C. Lu, P. K. Grimes, T.-J. Chen, Y.-P. Chang, C.-y. Tong, and M.-J. Wang, "A Silicon Chip-Based Waveguide Directional Coupler for Terahertz Applications," *IEEE Transactions on Terahertz Science and Technology*, vol. 10, no. 6, pp. 698–703, Nov. 2020. doi: 10.1109/TTHZ.2020.3022018 .

[12] H. Lees, B. Chung, and W. Withayachumnankul, "All-silicon 90-degree hybrid coupler for the WR3.4 band," in *2025 50th International Conference on Infrared, Millimeter, and Terahertz Waves (IRMMW-THz)*, 2025, pp. 1–2. doi: 10.1109/IRMMW-THz61557.2025.11319692 .

[13] J. Cabello-Sánchez, V. Drakinskiy, J. Stake, and H. Rodilla, "A Capacitive-Gap Coupled Terahertz Planar-Goubau-Line Power Divider," *IEEE Transactions on Terahertz Science and Technology*, vol. 13, no. 6, pp. 698–703, 2023. doi: 10.1109/TTHZ.2023.3303849 .

[14] L. Chen, W. Gao, C. Fumeaux, and W. Withayachumnankul, "Ultra-Compact Waveguide Couplers for All-Silicon Terahertz Platform," *Advanced Photonics Research*, vol. 7, no. 1, p. e202500247, 2026. doi: 10.1002/adpr.202500247 .

[15] J. L. Hesler and A. W. Lichtenberger, "THz Waveguide Couplers Using Quartz Micromachining," *21st International Symposium on Space Terahertz Technology*, 01 2010.

[16] IEEE, "IEEE Standard for Rectangular Metallic Waveguides and Their Interfaces for Frequencies of 110 GHz and Above—Part 1: Frequency Bands and Waveguide Dimensions," *IEEE Std 1785.1-2012*, pp. 1–22, 2013. doi: 10.1109/IEEESTD.2013.6471987 .

[17] A. Goturu, M. Dornieden, and J. Stake, "A planar 925-GHz branch line coupler," in *2025 50th International Conference on Infrared, Millimeter, and Terahertz Waves (IRMMW-THz)*, 2025, pp. 1–2. doi: 10.1109/IRMMW-THz61557.2025.11319720 .

[18] J. W. Kooi, G. Chattopadhyay, S. Withington, F. Rice, J. Zmuidzinas, C. Walker, and G. Yassin, "A Full-Height Waveguide to Thin-Film Microstrip Transition with Exceptional RF Bandwidth and Coupling Efficiency," *International Journal of Infrared and Millimeter Waves*, vol. 24, no. 3, pp. 261–284, Mar. 2003. doi: 10.1023/A:1021903132609 .
[19] R. Bass, J. Schultz, A. Lichtenberger, R. Weikle, S.-K. Pan, E. Bryerton, C. Walker, and J. Kooi, "Ultra-Thin Silicon Chips for Submillimeter-Wave Applications," *15th International Symposium on Space Terahertz Technology*, Jan. 2004.
[20] D. F. Edwards, "Silicon (Si)," in *Handbook of Optical Constants of Solids*, E. D. Palik, Ed. Boston: Academic Press, 1985, pp. 547–569. doi: 10.1016/B978-0-08-054721-3.50029-0 .
[21] N. Laman and D. Grischkowsky, "Terahertz conductivity of thin metal films," *Applied Physics Letters*, vol. 93, no. 5, p. 051105, 08 2008. doi: 10.1063/1.2968308 .
[22] D. Grischkowsky, S. Keiding, M. van Exter, and C. Fattinger, "Far-infrared time-domain spectroscopy with terahertz beams of dielectrics and semiconductors," *J. Opt. Soc. Am. B*, vol. 7, no. 10, pp. 2006–2015, Oct. 1990. doi: 10.1364/JOSAB.7.002006 .
[23] C. Zhang, "Development of Single-Ended and Balun Integrated Probes for THz Applications," in *PhD. thesis*, Sep. 2014. doi: 10.18130/V3WZ69 .
[24] A. B. Kaul, B. Bumble, K. A. Lee, H. G. LeDuc, F. Rice, and J. Zmuidzinas, "Fabrication of wide-IF 200–300GHz superconductor–insulator–superconductor mixers with suspended metal beam leads formed on silicon-on-insulator," *Journal of Vacuum Science & Technology B: Microelectronics and Nanometer Structures Processing, Measurement, and Phenomena*, vol. 22, no. 5, pp. 2417–2422, Oct. 2004. doi: 10.1116/1.1798831 .
[25] IEEE, "IEEE Standard for Rectangular Metallic Waveguides and Their Interfaces for Frequencies of 110 GHz and Above—Part 2: Waveguide Interfaces," *IEEE Std 1785.2-2016*, pp. 1–22, 2016. doi: 10.1109/IEEESTD.2016.7564020 .
[26] W. Kruppa and K. Sodomsky, "An Explicit Solution for the Scattering Parameters of a Linear Two-Port Measured with an Imperfect Test Set (Correspondence)," *IEEE Transactions on Microwave Theory and Techniques*, vol. 19, no. 1, pp. 122–123, 1971. doi: 10.1109/TMTT.1971.1127466 .
[27] M. Zeier, M. Wollensack, J. Hoffmann, P. Morrissey, J. Ruefenacht, and D. Stalder, "VNA Tools—A Metrology Software Supporting the Digital Traceability Chain," *Metrology*, vol. 5, no. 4, 2025. doi: 10.3390/metrology5040072 .
[28] J. Stenarson, K. Yhland, T. N. T. Do, H. Zhao, P. Sobis, and J. Stake, "Influence of waveguide width errors on TRL and LRL calibrations," in *79th ARFTG Microwave Measurement Conference*, 2012, pp. 1–3. doi: 10.1109/ARFTG79.2012.6291182 .
[29] D. Koller, S. Durant, E. Bryerton, J. Hesler, and A. Arsenovic, "Challenges of WM164 S-parameter measurements due to flange dimensional tolerances," in *2016 41st International Conference on Infrared, Millimeter, and Terahertz waves (IRMMW-THz)*, 2016, pp. 1–2. doi: 10.1109/IRMMW-THz.2016.7758491 .
[30] J. Skinner, D. Koller, H.-U. Nickel, N. M. Ridler, and S. Lucyszyn, "Derivation of Rectangular Metallic Waveguide Attenuation Constant for IEC 60153-2 and IEEE 1785.1 International Standards," *IEEE Transactions on Terahertz Science and Technology*, vol. 15, no. 4, pp. 734–737, 2025. doi: 10.1109/TTHZ.2025.3573847 .
[31] M. van Exter, C. Fattinger, and D. Grischkowsky, "Terahertz time-domain spectroscopy of water vapor," *Opt. Lett.*, vol. 14, no. 20, pp. 1128–1130, Oct. 1989. doi: 10.1364/OL.14.001128 .
[32] H. Ito, Y. Kawamoto, T. Nagatsuma, and T. Ishibashi, "Integrated Balanced Mixer for 300-GHz Band Based on Fermi-Level Managed Barrier Diode on Si Platform," in *2024 49th International Conference on Infrared, Millimeter, and Terahertz Waves (IRMMW-THz)*, 2024, pp. 1–2. doi: 10.1109/IRMMW-THz60956.2024.10697791 .
[33] P. H. Siegel, "THz Instruments for Space," *IEEE Transactions on Antennas and Propagation*, vol. 55, no. 11, pp. 2957–2965, 2007. doi: 10.1109/TAP.2007.908557 .
[34] T. W. Crowe, S. H. Jones, J. Stake, I. Mehdi, and N. Llombart, "In Memoriam of Jeffrey L. Hesler," *IEEE Transactions on Terahertz Science and Technology*, vol. 16, no. 2, pp. 88–89, 2026. doi: 10.1109/TTHZ.2026.3654821 .

Aditya Goturu received her M.Sc. degree in electrical engineering from Chalmers University of Technology in Gothenburg, Sweden, in 2025.

She is now pursuing her Ph.D. at the Terahertz and Millimetre Wave Laboratory, Chalmers University of Technology. Her research interests include the design of waveguide-based terahertz electronic circuits and terahertz metrology.

Malte Dornieden received his M.Sc. degree in Electrical Engineering from the Technical University of Berlin in 2017.

After several years in industrial research positions, he is currently pursuing his PhD at the Terahertz and Millimetre Wave Laboratory, where his research focuses on novel detector concepts for future terahertz wireless communication.

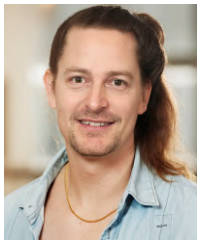

Jonathan Westin is a Research Engineer at the Terahertz and Millimetre Wave Laboratory, Department of Microtechnology and Nanoscience (MC2), Chalmers University of Technology, Gothenburg, Sweden. His work focuses on precision mechanical design and fabrication for high-frequency and terahertz research applications.

Jan Stake (Fellow, IEEE) was born in Uddevalla, Sweden, in 1971. He received an M.Sc. in electrical engineering and a Ph.D. in microwave electronics from Chalmers University of Technology in Gothenburg, Sweden, in 1994 and 1999, respectively.

In 1997, he was a Research Assistant at the University of Virginia, Charlottesville, VA, USA. From 1999 to 2001, he was a Research Fellow with the Millimetre Wave Group at the Rutherford Appleton Laboratory, Didcot, UK. He then joined Saab Combitech Systems AB, Gothenburg, Sweden, as a Senior RF/microwave Engineer until 2003. From 2000 to 2006, he held various academic positions at Chalmers University of Technology, and from 2003 to 2006, he also served as the Head of the Nanofabrication Laboratory in the Department of Microtechnology and Nanoscience (MC2). In 2006, he was appointed Professor and the Head of the Terahertz and Millimetre Wave Laboratory at Chalmers University of Technology. He was a Visiting Professor with the Submillimeter Wave Advanced Technology (SWAT) Group at Caltech/JPL, Pasadena, CA, USA, in 2007 and at TU Delft, the Netherlands, in 2020. He was appointed as a Visiting Fellow at the National Physical Laboratory in the UK in 2024. Additionally, he is the co-founder of Wasa Millimeter Wave AB, Gothenburg, Sweden. His research interests include high-frequency semiconductor devices, terahertz and far-infrared electronics, submillimeter wave measurement techniques, and terahertz systems.

Prof. Stake served as Editor-in-Chief of the IEEE Transactions on Terahertz Science and Technology from 2016 to 2018 and as Topical Editor from 2012 to 2015. From 2019 to 2021, he was chair of the IEEE THz Science and Technology Best Paper Award committee. He served on the International Society of Infrared, Millimeter, and Terahertz Waves (IRMMW-THz) organization committee from 2017 to 2024.